# 7

# Reflection seismology

One of the most important applications of seismology involves the probing of Earth's internal structure by examining energy reflected at steep incidence angles from subsurface layers. This technique may loosely be termed *reflection seismology* and has been used extensively by the mining and petroleum industries to study the shallow crust, generally using portable instruments and artificial sources. However, similar methods can be applied to the deeper Earth using recordings of earthquakes or large explosions. Because reflected seismic waves are sensitive to sharp changes in velocity or density, reflection seismology can often provide much greater lateral and vertical resolution than can be obtained from study of direct seismic phases such as $P$ and $S$ (analyses of these arrivals may be termed *refraction seismology*). However, mapping of reflected phases into reflector depths requires knowledge of the average background seismic velocity structure, to which typical reflection seismic data are only weakly sensitive. Thus refraction experiments are a useful complement to reflection experiments when independent constraints on the velocity structure (e.g., from borehole logs) are unavailable.

Reflection seismic experiments are typically characterized by large numbers of sources and receivers at closely spaced and regular intervals. Because the data volume generally makes formal inversions too costly for routine processing, more practical approximate methods have been widely developed to analyze the results. Simple time versus distance plots of the data can produce crude images of the subsurface reflectors; these images become increasingly accurate as additional processing steps are applied to the data.

Our discussion in this chapter will be limited to $P$-wave reflections, as the sources and receivers in most reflection seismic experiments are designed to produce and record $P$ waves. Our focus will also mainly be concerned with the travel time rather than the amplitude of seismic reflections. Although amplitudes are sometimes studied, historically amplitude information has assumed secondary importance in reflection processing. Indeed often amplitudes are self-scaled prior to plotting using *automatic gain control* (AGC) techniques. Finally, we will consider a two-dimensional geometry, for which the sources, receivers, and reflectors are assumed to lie within a vertical plane. Recently, an increasing number of reflection surveys involve a grid of sources and receivers on the surface that are capable of resolving three-dimensional Earth structure. Most of the concepts described in this chapter, such as common midpoint stacking and migration, are readily generalized to three dimensions, although the data volume and computational requirements are much greater in this case.

Reflection seismology is a big topic, and only a brief outline can be presented here. For additional details, the reader is referred to texts such as Yilmaz (1987), Sheriff and Geldart (1995), and Claerbout (1976, 1985).

## 7.1 Zero-offset sections

Consider a collocated source and receiver at the surface above a horizontally layered velocity structure (Fig. 7.1). The downward propagating $P$ waves from the source are reflected upward by each of the interfaces. The receiver will record a series of pulses at times determined by the two-way $P$ travel time between the surface and the interfaces. If the velocity structure is known, these times can easily be converted to depths.

Now imagine repeating this as the source and receiver are moved to a series of closely spaced points along the surface. At each location, the receiver records the reflected waves from the underlying structure. By plotting the results as a function of time and distance, an image can be produced of the subsurface structure (Fig. 7.2). For convenience in interpreting the results, these record sections are plotted with downward increasing time (i.e., upside down compared with the plots

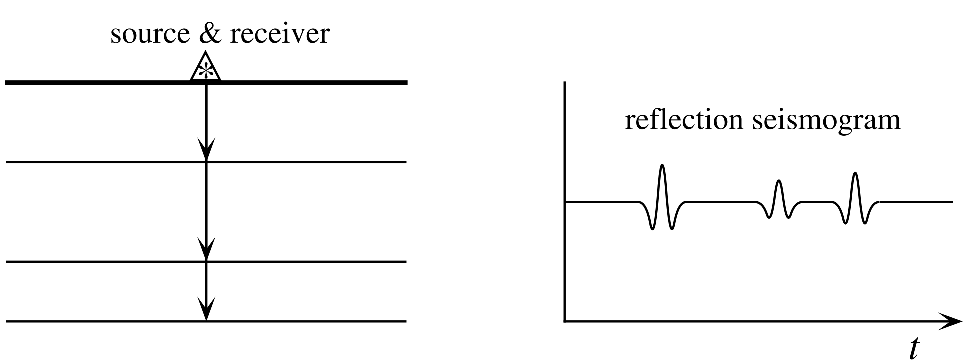


**Figure 7.1** Seismic waves from a surface source are reflected by subsurface layers, producing a seismogram with discrete pulses for each layer. In this example, the velocity contrasts at the interfaces are assumed to be small enough that multiple reflections can be ignored.

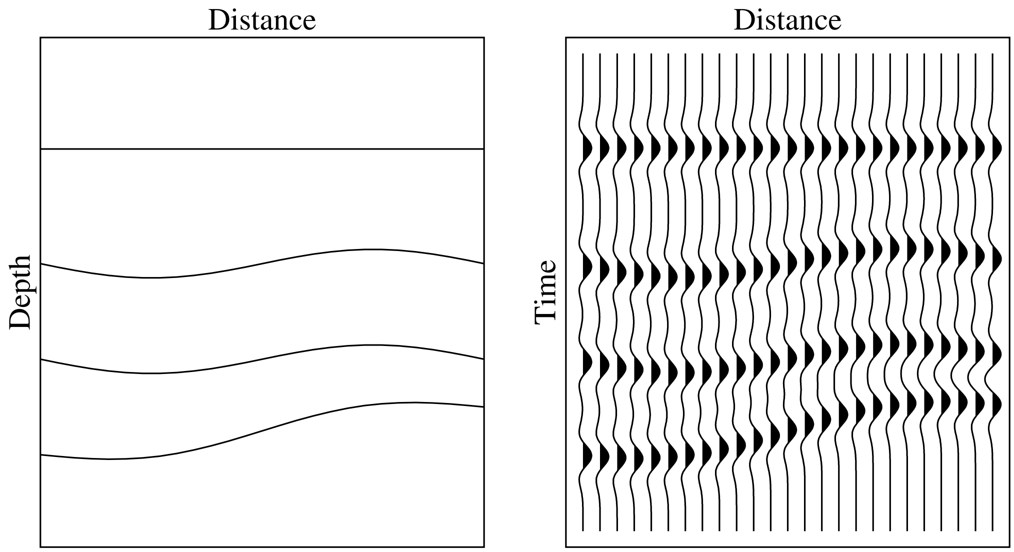


**Figure 7.2** The structural cross-section on the left is imaged by an idealized zero-offset seismic reflection profile on the right. Here we have assumed that velocity is approximately constant throughout the model (except for thin reflecting layers) so that time and depth scale linearly.

in Chapter 4). Another convention, commonly used in reflection seismology, is to darken the positive areas along the seismograms, increasing the visibility of the reflected pulses.

If the large-scale $P$ velocity is constant throughout the region of interest, then time in this image scales linearly with depth and we can readily convert the vertical axis to depth. If velocity increases with depth, a somewhat more complicated transformation is necessary. Because the velocity structure is often not known very accurately, most reflection seismic results are plotted as time sections, rather than depth sections.

This example is termed a *zero-offset section* because there is assumed to be no separation between the sources and receivers. More generally, reflection data are recorded at a variety of source–receiver offsets, but the data are processed in order to produce an equivalent zero-offset section that is easier to interpret than the original data. In the idealized example shown in Figure 7.2, the zero-offset section provides a clear, unbiased image of the reflectors. However, in practice there are several factors that can hinder construction and interpretation of such a section:

1. Single records are often noisy and zero-offset data may be contaminated by near-source reverberations. Improved results may be obtained by including different source–receiver offsets to increase the number of data and then averaging or *stacking* the records to increase the signal-to-noise ratio of the reflected pulses.
2. The layer spacing may be short compared to the source duration, producing overlapping arrivals that make it difficult to distinguish the individual reflectors. This may

be addressed through a process termed *deconvolution*, which involves removing the properties of the source from the records, providing a general sharpening of the image.

3. Lateral variations in structure or dipping layers may result in energy being scattered away from purely vertical ray paths. These arrivals can bias estimates of reflector locations and depths. By summing along possible sources of scattered energy, it is possible to correct the data for these effects; these techniques are termed *migration* and can result in a large improvement in image quality.
4. Uncertainties in the overall velocity structure may prevent reliable conversion between time and depth and hinder application of stacking and migration techniques. Thus it is critical to obtain the most accurate velocity information possible; in cases where outside knowledge of the velocities are unavailable, the velocities must be estimated directly from the reflection data.

We now discuss each of these topics in more detail.

## 7.2 Common midpoint stacking

Consider a source recorded by a series of receivers at increasing distance. A pulse reflected from a horizontal layer will arrive earliest for the zero-offset receiver, while the arrivals at longer ranges will be delayed (Fig. 7.3). If the layer has thickness $h$ and a uniform $P$ velocity of $v$, then the minimum travel time, $t_0$, defined by the two-way vertical ray path, is

$$t_0 = \frac{2h}{v}. \tag{7.1}$$

More generally, the travel time as a function of range, $x$, may be expressed as

$$t(x) = \frac{2d}{v}, \tag{7.2}$$

where $d$ is the length of each leg of the ray path within the layer. From the geometry, we have

$$\begin{aligned} d^2 &= h^2 + (x/2)^2, \\ 4d^2 &= 4h^2 + x^2. \end{aligned} \tag{7.3}$$

Squaring (7.2) and substituting for $4d^2$, we may write

$$v^2 t^2 = x^2 + 4h^2 \tag{7.4}$$

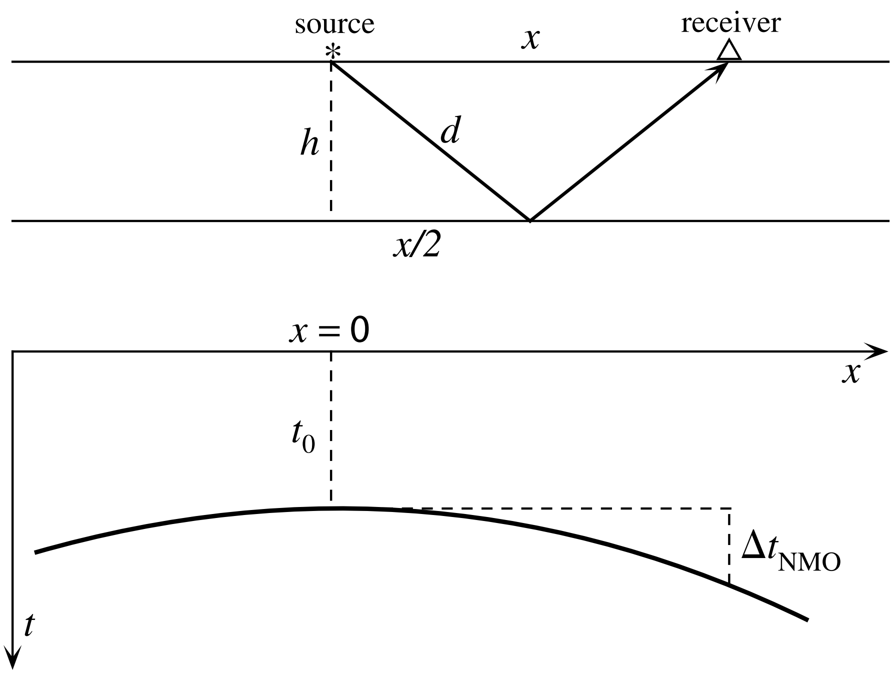


**Figure 7.3** A reflected ray path (top) and the corresponding travel time curve as a function of source–receiver separation (bottom). For a constant velocity model, the travel times form a hyperbola.

or

$$\frac{v^2 t^2}{4h^2} - \frac{x^2}{4h^2} = 1, \tag{7.5}$$

and we see that the travel time curve has the form of a hyperbola with the apex at $x = 0$. This is often expressed in terms of $t_0$ rather than $h$ by substituting $4h^2 = v^2 t_0^2$ from (7.1) to obtain

$$\frac{t^2}{t_0^2} - \frac{x^2}{v^2 t_0^2} = 1. \tag{7.6}$$

Solving for $t$ we have

$$\begin{aligned} t(x) &= \sqrt{t_0^2 + \frac{x^2}{v^2}} \\ &= t_0 \sqrt{1 + \left(\frac{x}{v t_0}\right)^2}. \end{aligned} \tag{7.7}$$

For small offsets ($x \ll vt_0$) we may approximate the square root as

$$t(x) \approx t_0\left[1 + \tfrac{1}{2}(x/vt_0)^2\right]. \tag{7.8}$$

The difference in time between the arrival at two different distances is termed the *moveout* and may be expressed as

$$\Delta t = t(x_2) - t(x_1) = t_0\sqrt{1 + (x_2/vt_0)^2} - t_0\sqrt{1 + (x_1/vt_0)^2} \tag{7.9}$$

$$\approx t_0\left[1 + \tfrac{1}{2}(x_2/vt_0)^2\right] - t_0\left[1 + \tfrac{1}{2}(x_1/vt_0)^2\right]$$

$$\approx \frac{x_2^2 - x_1^2}{2v^2 t_0}, \tag{7.10}$$

where the approximate form is valid at small offsets. The *normal moveout* (NMO) is defined as the moveout from $x = 0$ and is given by

$$\Delta t_{\mathrm{NMO}} = t_0\sqrt{1 + (x/vt_0)^2} - t_0 \tag{7.11}$$

$$\approx \frac{x^2}{2v^2 t_0}. \tag{7.12}$$

These equations are applicable for a single homogeneous layer. More complicated expressions can be developed for a series of layers overlying the target reflector or for dipping layers (e.g., see Sheriff and Geldart, 1995). Alternatively, the ray tracing theory developed in Chapter 4 can be applied to solve for the surface-to-reflector travel time for any arbitrary velocity versus depth function $v(z)$. Thus, a general form for the NMO equation is

$$\Delta t_{\mathrm{NMO}}(x) = 2[t(z, x/2) - t(z, 0)], \tag{7.13}$$

where $t(z, x)$ is the travel time from the surface to a point at depth $z$ and horizontal offset $x$.

A typical seismic reflection experiment deploys a large number of seismometers to record each source (these instruments are often called *geophones* in these applications, or *hydrophones* in the case of pressure sensors for marine experiments). This is repeated for many different source locations. The total data set thus consists of $nm$ records, where $n$ is the number of instruments and $m$ is the number of sources. The arrival time of reflectors on each seismogram depends on the source–receiver offset as well as the reflector depth. To display these results on a single plot, it is desirable to combine the data in a way that removes the offset dependence in the travel times so that any lateral variability in reflector depths can be seen clearly.

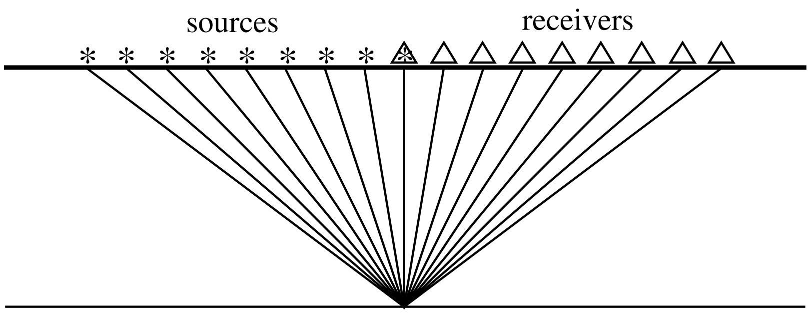


**Figure 7.4** The source and receiver locations for a common midpoint (CMP) gather.

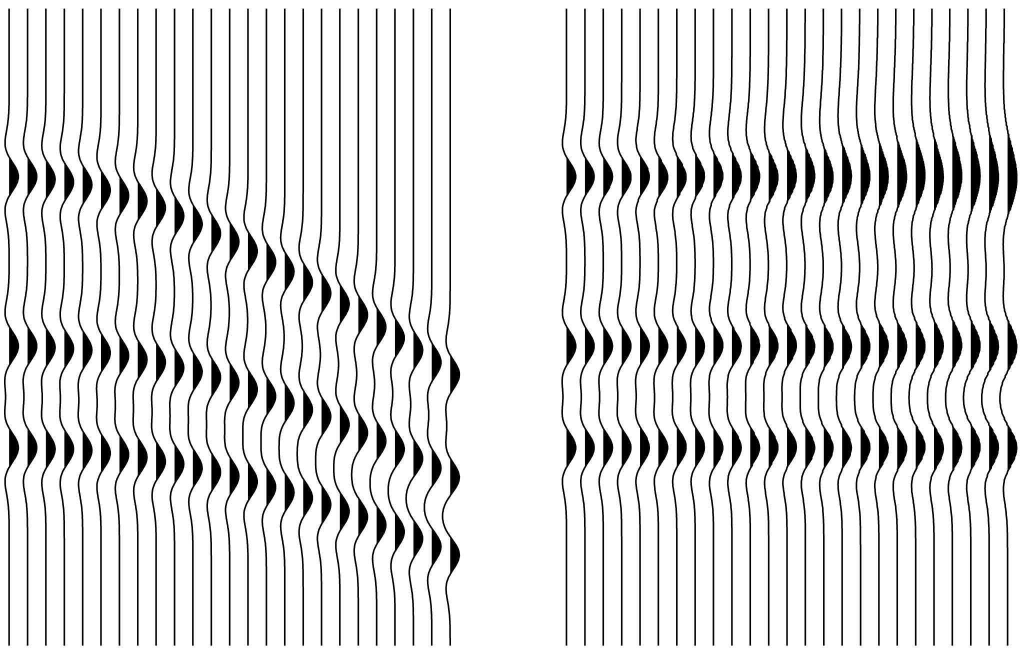

**Figure 7.5** The left plot shows reflection seismograms at increasing source–receiver distance. The right plot shows the same profile after applying a NMO correction to each time series. Note that this removes the range dependence in the arrival times. The NMO corrected records can then be stacked to produce a single composite zero-offset record.

This is done by summing subsets of the data along the predicted NMO times to produce a composite zero-offset profile. Data are generally grouped by predicted reflector location as illustrated in Figure 7.4.

Seismograms with common source–receiver midpoints are selected into what is termed a *gather*. A NMO correction is then applied to the records that shifts the times to their zero-offset equivalent (as illustrated in Fig. 7.5). Notice that this correction is not constant for each record but varies with time within the trace. This results in pulse broadening for the waveforms at longer offsets, but for short pulse lengths and small offsets this effect is not large enough to cause problems. Finally the NMO corrected data are summed and averaged to produce a single composite record that represents the zero-offset profile at the midpoint location. This is called *common midpoint (CMP) stacking*, or sometimes common depth point (CDP) stacking. The number of records, $n$, that are stacked is called the *fold*. For data with random noise, stacking can improve the signal-to-noise ratio of the records by a factor of $\sqrt{n}$. CMP stacking can also minimize the influence of contaminating arrivals, such as direct body waves or surface waves (Rayleigh waves, termed *ground roll* by reflection seismologists, are often the strongest arrival in reflection records), that do not travel along the predicted NMO travel time curves and thus do not stack coherently.

CMP stacking has proven to be very successful in practice and is widely used to produce reflection profiles at a minimum of computational expense. However, it requires knowledge of the velocity-depth function to compute the NMO times and it does not explicitly account for the possibility of energy reflected or scattered from non-horizontal interfaces. We will discuss ways to address some of these limitations later in this chapter, but first we examine source effects.

## 7.3 Sources and deconvolution

The ideal source for reflection seismology would produce a delta function or a very short impulsive wavelet that would permit closely spaced reflectors to be clearly resolved. In practice, however, more extended sources must be used and the finite source durations can cause complications in interpreting the data. For example, an airgun is often used for marine seismic reflection profiling. This device is towed behind a ship and fires bursts of compressed air at regular intervals. This creates a bubble that oscillates for several cycles before dissipating, producing a complicated "ringy" source-time function (e.g., Fig. 7.6). The reflection seismograms produced by such a source will reproduce this source-time function for each reflector. This is not too confusing in the case where there are only a few, widely separated reflectors. However, if several closely spaced reflectors are present then it becomes difficult to separate the real structure from the source.

The combination of the Earth response with the source-time function is termed *convolution* (see Appendix E) and may be written as

$$u(t) = s(t) * G(t) \equiv \int_0^{t_s} s(\tau)G(t-\tau)\,d\tau, \tag{7.14}$$

where $u(t)$ is the recorded seismogram, $s(t)$ is the effective source-time function (i.e., what is actually recorded by the receiver; we assume that $s(t)$ includes the receiver response and any near-source attenuation), $G(t)$ is the Earth response,

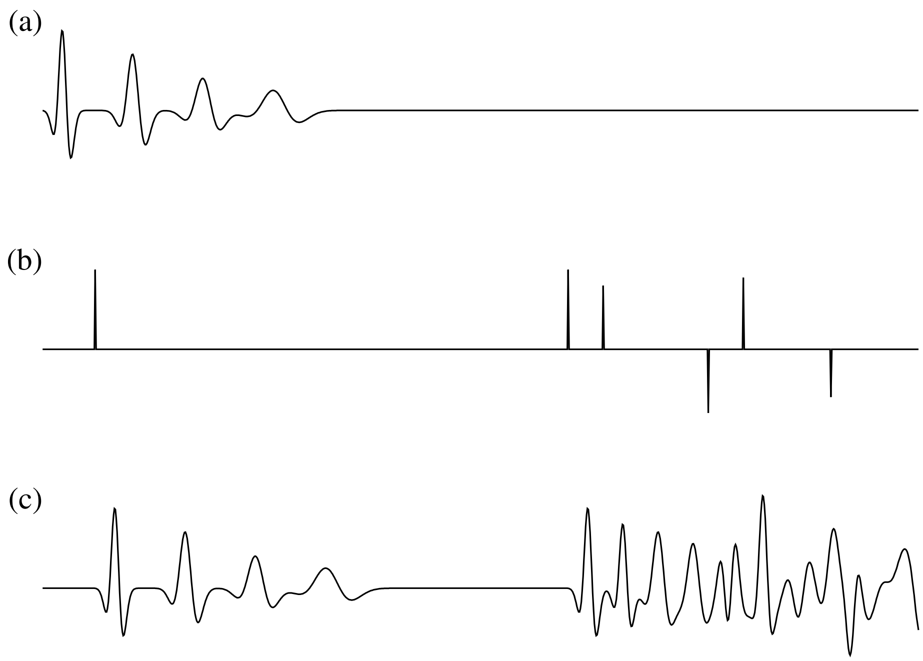


**Figure 7.6** (a) A schematic example of a typical source-time function $s(t)$ produced by an airgun in a marine experiment. A series of bubble pulses are produced by pressure reverberations within the water. (b) An idealized example of the Earth response function $G(t)$ showing a number of reflected pulses. (c) The result of convolving (a) and (b). While single isolated reflectors can still be identified, closely spaced reflectors produce a complex time series that cannot easily be unraveled.

and $t_s$ is the duration of the source. Recovering $G(t)$ from $u(t)$ in this case is termed *deconvolution* and is often an important part of reflection seismic processing. However, it is not always clear how best to perform deconvolution and this has been the subject of considerable research. The problem appears simpler in the frequency domain (see Appendix E) where convolution is expressed as a product, that is,

$$u(\omega) = s(\omega)G(\omega), \tag{7.15}$$

where $u(\omega)$, $s(\omega)$, and $G(\omega)$ are the Fourier transforms of $u(t)$, $s(t)$, and $G(t)$. Thus, in principle, frequency-domain deconvolution is straightforward:

$$G(\omega) = \frac{u(\omega)}{s(\omega)}. \tag{7.16}$$

The desired time series $G(t)$ can then be obtained from the inverse Fourier transform of $G(\omega)$. The difficulty with this approach is that (7.16) is exact and stable only for noiseless data and when $s(\omega)$ does not go to zero. In practice, some noise is present and the effective source-time function is usually band-limited so that $s(\omega)$ becomes very small at the low- and high-frequency limits. These complications can cause (7.16) to become unstable or produce artifacts in the deconvolved waveform. To address these difficulties, various methods for stabilizing deconvolution have been developed. Often a time-domain approach is more efficient for data processing, in which case a filter is designed to perform the deconvolution directly on the data.

Although deconvolution is an important part of reflection data processing, no deconvolution method is perfect, and some information is invariably lost in the process of convolution with the source-time function that cannot be recovered. For this reason, it is desirable at the outset to obtain as impulsive a source-time function as possible. Modern marine profiling experiments use airgun arrays that are designed to minimize the amplitudes of the later bubble pulses, resulting in much cleaner and less ringy pulses than the example plotted in Figure 7.6a.

Another important source-time function is produced by a machine that vibrates over a range of frequencies. This is the most common type of source for shallow crustal profiling on land and is termed *vibroseis* after the first commercial application of the method. The machine produces ground motion of the form of a modulated sinusoid, termed a *sweep*,

$$v(t) = A(t)\sin[2\pi(f_0 + bt)t]. \tag{7.17}$$

The amplitude $A(t)$ is normally constant except for a taper to zero at the start and end of the sweep. The sweep lasts from about 5 to 40 s with frequencies ranging from about 10 to 60 Hz. The sweep duration is long enough compared with the interval between seismic reflections that raw vibroseis records are difficult to interpret. To obtain clearer records, the seismograms, $u(t)$, are cross-correlated with the vibroseis sweep function.

The cross-correlation $f(t)$ between two real functions $a(t)$ and $b(t)$ is defined as

$$f(t) = a(t) \star b(t) = \int_{-\infty}^{\infty} a(\tau - t)b(\tau)\,d\tau, \tag{7.18}$$

where, following Bracewell (1978), we use the five-pointed star symbol $\star$ to denote cross-correlation; this should not be confused with the asterisk $*$ that indicates convolution. The cross-correlation integral is very similar to the convolution integral but without the time reversal of (7.14). Note that

$$a(t) * b(t) = a(-t) \star b(t) \tag{7.19}$$

and that, unlike convolution, cross-correlation is not commutative:

$$a(t) \star b(t) \neq b(t) \star a(t). \tag{7.20}$$

Cross-correlation of the vibroseis sweep function $v(t)$ with the original seismogram $u(t)$ yields the processed time series $u'(t)$:

$$u'(t) = v(t) \star u(t) = \int_0^{t_s} v(\tau - t)u(\tau)\, d\tau, \tag{7.21}$$

where $t_s$ is the sweep duration. From (7.14) and replacing $s(t)$ with $v(t)$, we obtain

$$\begin{aligned} u'(t) &= v(t) \star [v(t) * G(t)] && (7.22)\\ &= v(-t) * [v(t) * G(t)] && (7.23)\\ &= [v(-t) * v(t)] * G(t) && (7.24)\\ &= [v(t) \star v(t)] * G(t) && (7.25)\\ &= v'(t) * G(t), && (7.26) \end{aligned}$$

where we have used (7.19) and the associative rule for convolution. The cross-correlation of $v(t)$ with itself, $v'(t) = v(t) \star v(t)$, is termed the *autocorrelation* of $v(t)$. This is a symmetric function, centered at $t = 0$, that is much more sharply peaked than $v(t)$. Thus, by cross-correlating the recorded seismogram with the vibroseis sweep function $v(t)$, one obtains a time series that represents the Earth response convolved with an effective source that is relatively compact. These relationships are illustrated in Figure 7.7. Cross-correlation with the source function is a simple form of deconvolution that is sometimes termed *spiking deconvolution*. Notice that the resulting time series is only an approximation to the desired Earth response function $G(t)$. More sophisticated methods of deconvolution can achieve better results, but $G(t)$ can never be recovered perfectly since $v(t)$ is band-limited and the highest and lowest frequency components of $G(t)$ are lost in the convolution.

## 7.4 Migration

Up to this point, we have modeled reflection seismograms as resulting from reflections off horizontal interfaces. However, in many cases lateral variations in structure are present; indeed, resolving these features is often a primary goal of reflection profiling. Dipping, planar reflectors can be accommodated by modifying the NMO equations to adjust for differences between the updip and downdip directions. However, more complicated structures will produce scattered and diffracted arrivals that cannot be modeled by simple plane-wave reflections, and accurate interpretation

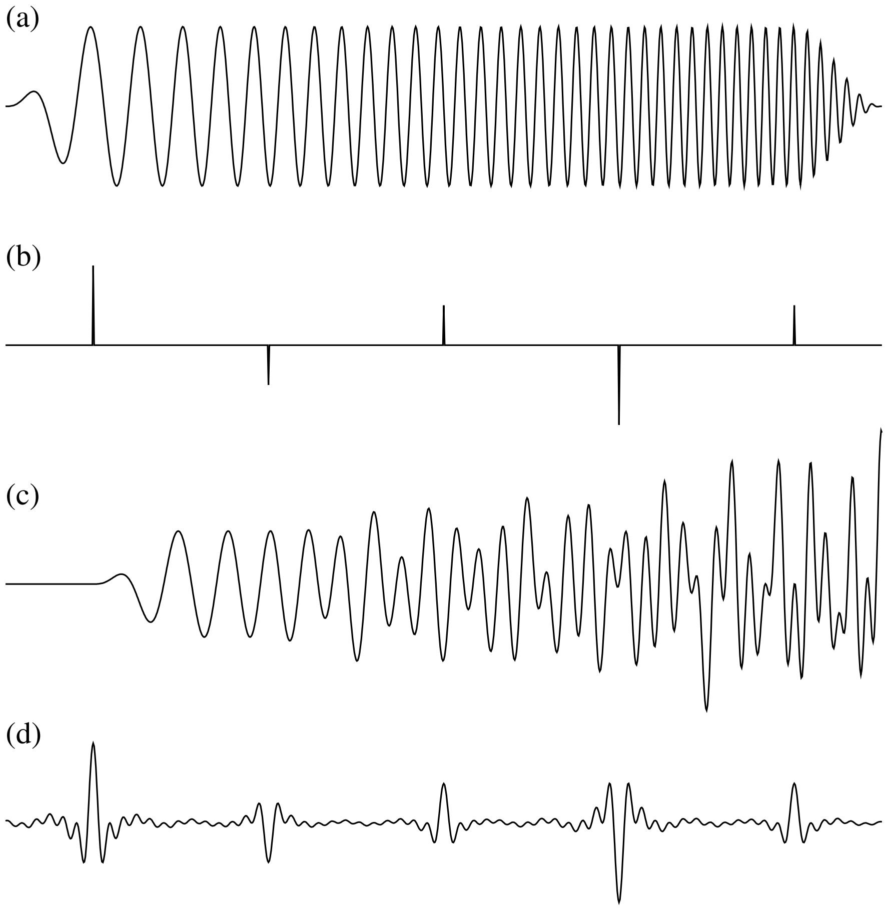


**Figure 7.7** (a) An example of a vibroseis sweep function $v(t)$. (b) A hypothetical Earth response function $G(t)$. (c) The result of convolving (a) and (b). (d) The result of cross-correlating (a) with (c).

of data from such features requires a theory that takes these arrivals into account. Most of the analysis techniques developed for this purpose are based on the idea that velocity perturbations in the medium can be thought of as generating secondary seismic sources in response to the incident wavefield, and the reflected wavefield can be modeled as a sum of these secondary wavelets.

### 7.4.1 Huygens' principle

Huygens' principle, first described by Christiaan Huygens (*c*. 1678), is most commonly mentioned in the context of light waves and optical ray theory, but it is applicable to any wave propagation problem. If we consider a plane wavefront traveling in a homogeneous medium, we can see how the wavefront can be thought to propagate through the constructive interference of secondary wavelets (Fig. 7.8). This simple idea provides, at least in a qualitative sense, an explanation for the behavior of waves when they pass through a narrow aperture.

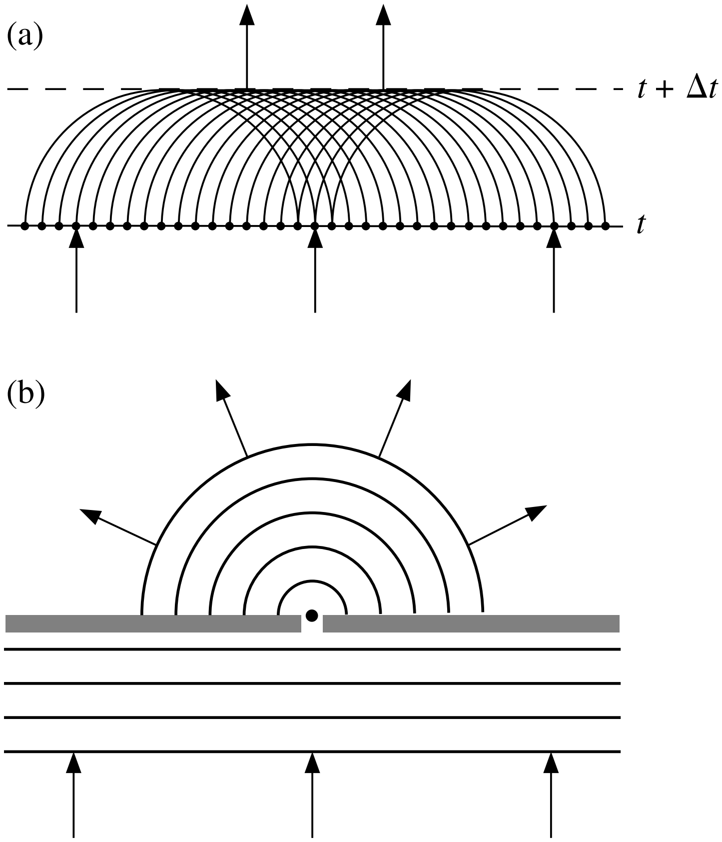


**Figure 7.8** Illustrations of Huygens' principle. (a) A plane wave at time $t + \Delta t$ can be modeled as the coherent sum of the spherical wavefronts emitted by point sources on the wavefront at time $t$. (b) A small opening in a barrier to incident waves will produce a diffracted wavefront if the opening is small compared to the wavelength.

The bending of the ray paths at the edges of the gap is termed *diffraction*. The degree to which the waves diffract into the "shadow" of the obstacle depends upon the wavelength of the waves in relation to the size of the opening. At relatively long wavelengths (e.g., ocean waves striking a hole in a jetty), the transmitted waves will spread out almost uniformly over 180°. However, at short wavelengths the diffraction from the edges of the slot will produce a much smaller spreading in the wavefield. For light waves, very narrow slits are required to produce noticeable diffraction. These properties can be modeled using Huygens' principle by computing the effects of constructive and destructive interference at different wavelengths.

### 7.4.2 Diffraction hyperbolas

We can apply Huygens' principle to reflection seismology by imagining that each point on a reflector generates a secondary source in response to the incident wavefield. This is sometimes called the "exploding reflector" model. Consider a single point scatterer in a zero-offset section (Fig. 7.9). The minimum travel time is given by

$$t_0 = \frac{2h}{v}, \tag{7.27}$$

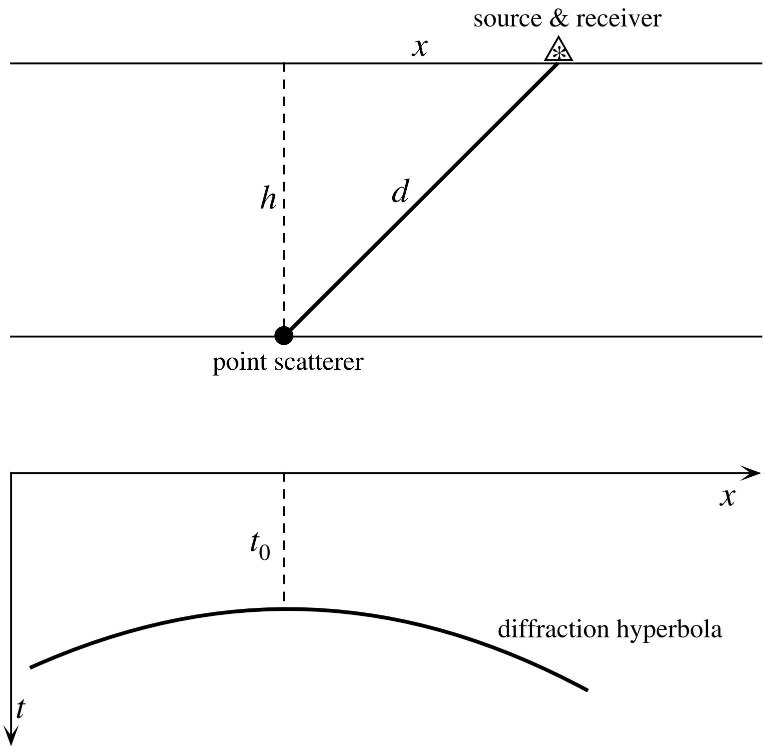


**Figure 7.9** A point scatterer will produce a curved "reflector" in a zero-offset section.

where $h$ is the depth of the scatterer and $v$ is the velocity (assumed constant in this case). More generally, the travel time as a function of horizontal distance, $x$, is given by

$$t(x) = \frac{2\sqrt{x^2 + h^2}}{v}. \tag{7.28}$$

Squaring and rearranging, this can be expressed as

$$\frac{v^2 t^2}{4h^2} - \frac{x^2}{h^2} = 1 \tag{7.29}$$

or

$$\frac{t^2}{t_0^2} - \frac{4x^2}{v^2 t_0^2} = 1 \tag{7.30}$$

after substituting $4h^2 = v^2 t_0^2$ from (7.27). The travel time curve for the scattered arrival has the form of a hyperbola with the apex directly above the scattering point. Note that this hyperbola is steeper and results from a different ray geometry than the NMO hyperbola discussed in Section 7.2 (equation (7.5)). The NMO hyperbola describes travel time for a reflection off a horizontal layer as a function of source–receiver distance; in contrast (7.30) describes travel time as a function of distance

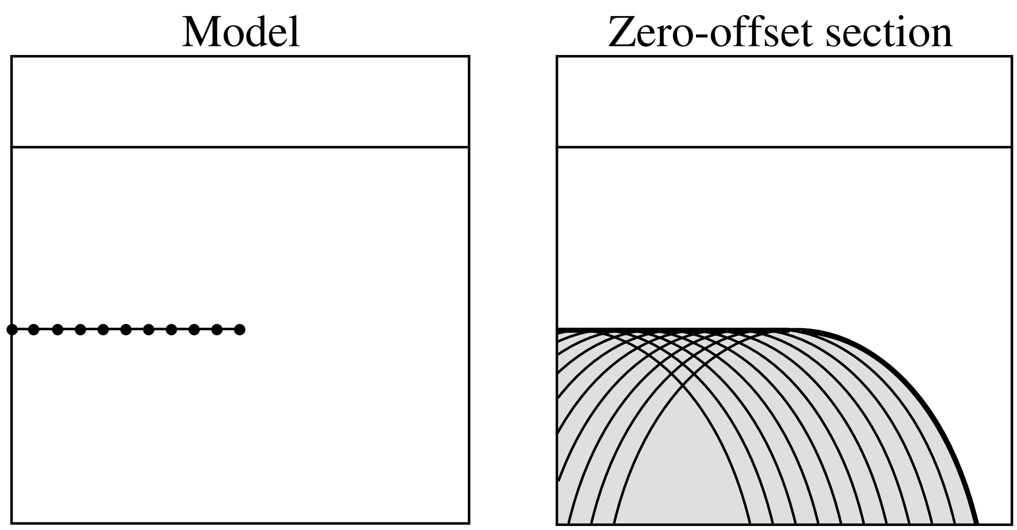


**Figure 7.10** The endpoint of a horizontal reflector will produce a diffracted arrival in a zero-offset section. The reflector itself can be modeled as the coherent sum of the diffraction hyperbola from individual point scatterers. The diffracted phase, shown as the curved heavy line, occurs at the boundary of the region of scattered arrivals.

away from a point scatterer at depth for zero-offset data (the source and receiver are coincident).

### 7.4.3 Migration methods

Consider a horizontal reflector that is made up of a series of point scatterers, each of which generates a diffraction hyperbola in a zero-offset profile (Fig. 7.10). Following Huygens' principle, these hyperbolas sum coherently only at the time of the main reflection; the later contributions cancel out. However, if the reflector vanishes at some point, then there will be a diffracted arrival from the endpoint that will show up in the zero-offset data. This creates an artifact in the section that might be falsely interpreted as a dipping, curved reflector.

Techniques for removing these artifacts from reflection data are termed *migration* and a number of different approaches have been developed. The simplest of these methods is termed *diffraction summation migration* and involves assuming that each point in a zero-offset section is the apex of a hypothetical diffraction hyperbola. The value of the time series at that point is replaced by the average of the data from adjacent traces taken at points along the hyperbola. In this way, diffraction artifacts are "collapsed" into their true locations in the migrated section. In many cases migration can produce a dramatic improvement in image quality (e.g., Fig. 7.11).

A proper implementation of diffraction summation migration requires wave propagation theory that goes beyond the simple ideas of Huygens' principle. In particular, the scattered amplitudes vary as a function of range and ray angle, and the

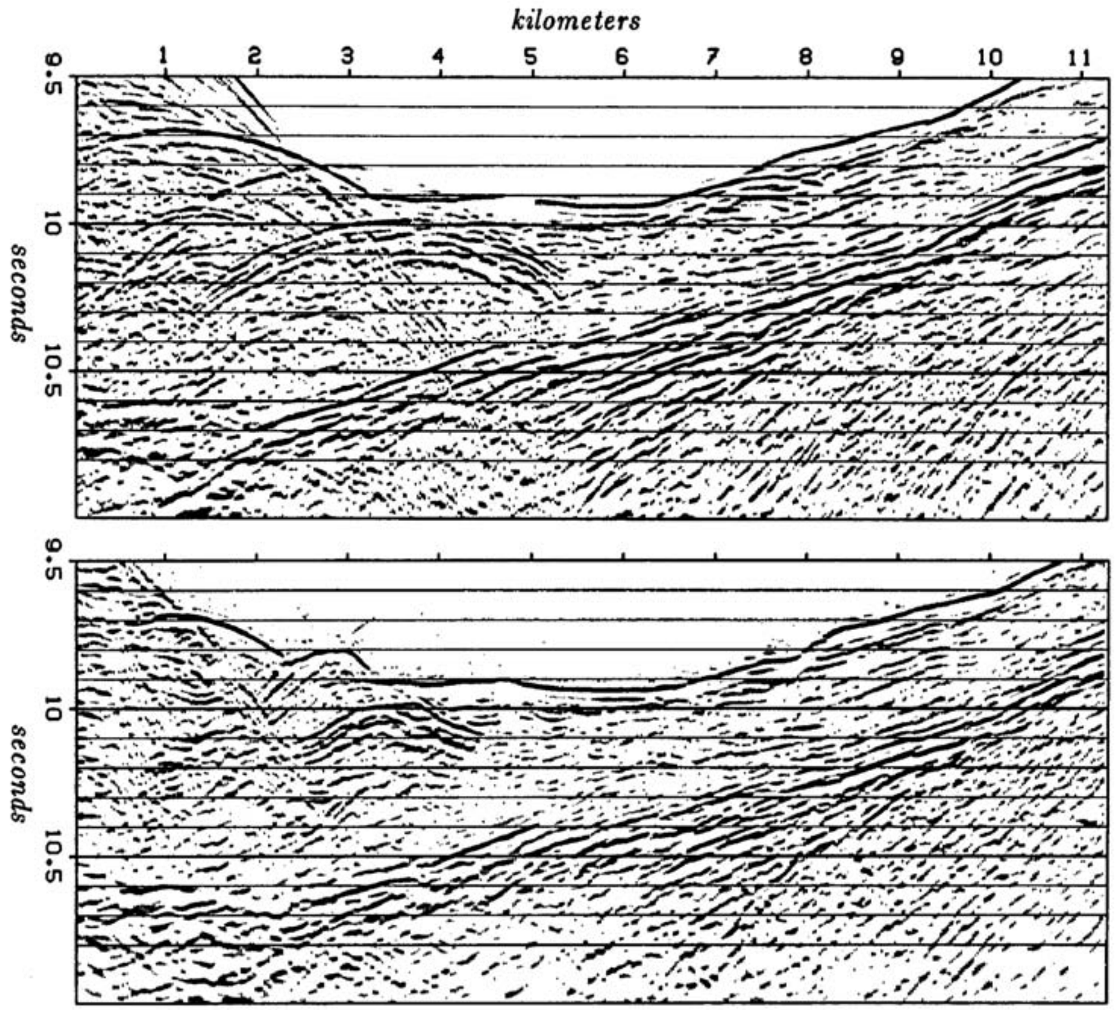


**Figure 7.11** Original (top) and migrated (bottom) reflection data from a survey line across the Japan trench (figure modified from Claerbout, 1985; data from the Tokyo University Oceanographic Research Institute).

Huygens secondary sources are given, for a three-dimensional geometry, by the time derivative of the source-time function (in the frequency domain this is described by the factor $-i\omega$, a $\pi/2$ (90-degree) phase shift with amplitude proportional to frequency). In the case of a two-dimensional geometry, the secondary sources are the "half-derivative" of the source function (a 45-degree phase shift with amplitude scaled by the square root of frequency). These details are provided by Kirchhoff theory, which is discussed later in this chapter. The diffraction hyperbola equation assumes a uniform velocity structure, but migration concepts can be generalized to more complicated velocity models. However, it is important to have an accurate velocity model, as use of the wrong model can result in "undermigrated" or "overmigrated" sections.

In common practice, data from seismic reflection experiments are first processed into zero-offset sections through CMP stacking. The zero-offset section is then migrated to produce the final result. This is termed *poststack migration*. Because CMP stacking assumes horizontal layering and may blur some of the details of the original data, better results can be obtained if the migration is performed prior to stacking. This is called *prestack migration*. Although prestack migration is known to produce superior results, it is not implemented routinely owing to its much greater computational cost.

## 7.5 Velocity analysis

Knowledge of the large-scale background seismic velocity structure is essential for reflection seismic processing (for both stacking and migration) and for translating observed events from time to depth. Often this information is best obtained from results derived independently of the reflection experiment, such as from borehole logs or from a collocated refraction experiment. However, if such constraints are not available a velocity profile must be estimated from the reflection data themselves. This can be done in several different ways.

One approach is to examine the travel time behavior of reflectors in CMP gathers. From (7.7), we have for a reflector overlain by material of uniform velocity $v$:

$$t^2(x) = t_0^2 + \frac{x^2}{v^2} \tag{7.31}$$

$$= t_0^2 + u^2x^2, \tag{7.32}$$

where $u = 1/v$ is the slowness of the layer. From observations of the NMO offsets in a CMP gather, one can plot values of $t^2$ versus $x^2$. Fitting a straight line to these points then gives the intercept $t_0^2$ and the slope $u^2 = 1/v^2$. Velocity often is not constant with depth, but this equation will still yield a velocity, which can be shown to be approximately the root-mean-square (rms) velocity of the overlying medium, that is, for $n$ layers

$$v^2 \approx \frac{\sum_{i=1}^{n} v_i^2 \Delta t_i}{\sum_{i=1}^{n} \Delta t_i}, \tag{7.33}$$

where $\Delta t_i$ is the travel time through the $i$th layer.

Another method is to plot NMO corrected data as a function of offset for different velocity models to see which model best removes the range dependence in the data or produces the most coherent image following CMP stacking. As in the case of the

$t^2(x^2)$ plotting method, this will only resolve the velocities accurately if a reasonable spread in source–receiver offsets are available. Zero-offset data have no direct velocity resolution; the constraints on velocity come from the NMO offsets in the travel times with range. Thus, wider source–receiver profiling generally produces better velocity resolution, with the best results obtained in the case where receiver ranges are extended far enough to capture the direct refracted phases. However, even zero-offset data can yield velocity information if diffraction hyperbolas are present in the zero-offset profiles, as the curvature of these diffracted phases can be used to constrain the velocities. One approach is to migrate the section with different migration velocities in order to identify the model that best removes the artifacts in the profile.

### 7.5.1 Statics corrections

Often strong near-surface velocity heterogeneity produces time shifts in the records that can vary unpredictably between sources and stations. This could be caused by topography/bathymetry or a sediment layer of variable thickness. The resulting "jitter" in the observed reflected pulses (Fig. 7.12) can hinder application of stacking and migration techniques and complicate interpretation of the results. Thus, it is desirable to remove these time shifts prior to most processing of the results. This is done by applying timing corrections, termed *statics corrections*, to the data. In the case of the receivers, these are analogous to the station terms (the

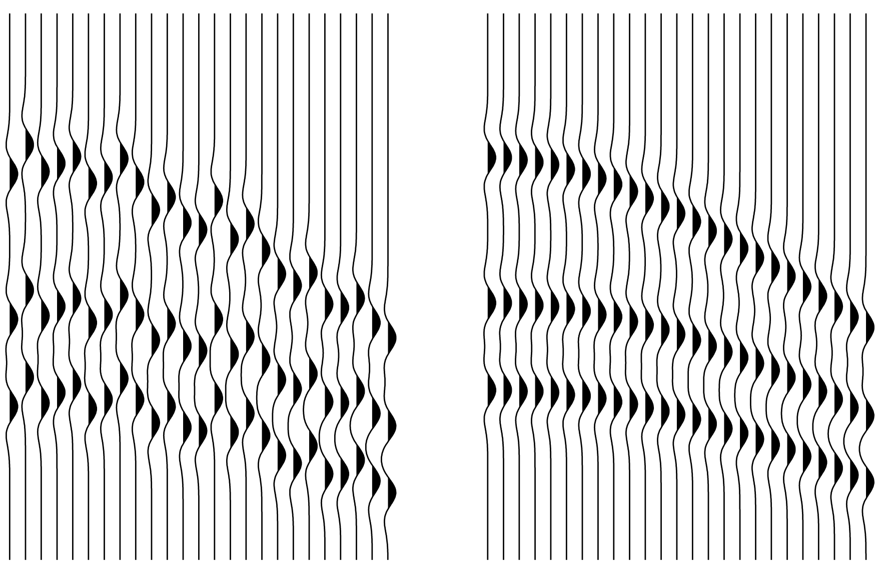

**Figure 7.12** Small time shifts on individual records produce offsets in reflectors in CMP gathers (left plot) that prevent coherent stacking of these phases in data processing. These shifts can be removed by applying static corrections (right plot).

average travel time residual at a particular station for many different events) used in travel time inversions for Earth structure. Statics may be computed by tracking the arrival time of a reference phase, such as a refracted arrival. Often automatic methods are applied to find the time shifts that best smooth the observed reflectors. The goal is to shift the timing of the individual records such that reflectors will stack coherently. This problem is tractable since the time shifts are generally fairly small, and solutions for the time shifts are overdetermined in typical reflection experiments (multiple receivers for each source, multiple sources for each receiver).

## 7.6 Receiver functions

A wide-used technique in global seismology that has many parallels to reflection seismology is the seismic *receiver function* (Langston, 1977). The method exploits the fact that upcoming $P$ waves beneath seismic stations will generate $P$-to-$S$ converted phases at any sharp interfaces below the receiver. This $SV$-polarized wave is termed the $Ps$ phase (see Figure 7.13) and will follow the direct $P$ phase by a time that increases with the depth of the interface.

Thus in principle we could estimate the depth of the discontinuity from the $Ps-P$ time, but in practice $Ps$ is only rarely observed clearly on individual seismograms because it is usually obscured by the coda of the $P$ wave. However, $Ps$ should have the same shape as the direct $P$ pulse (essentially the source-time function of the

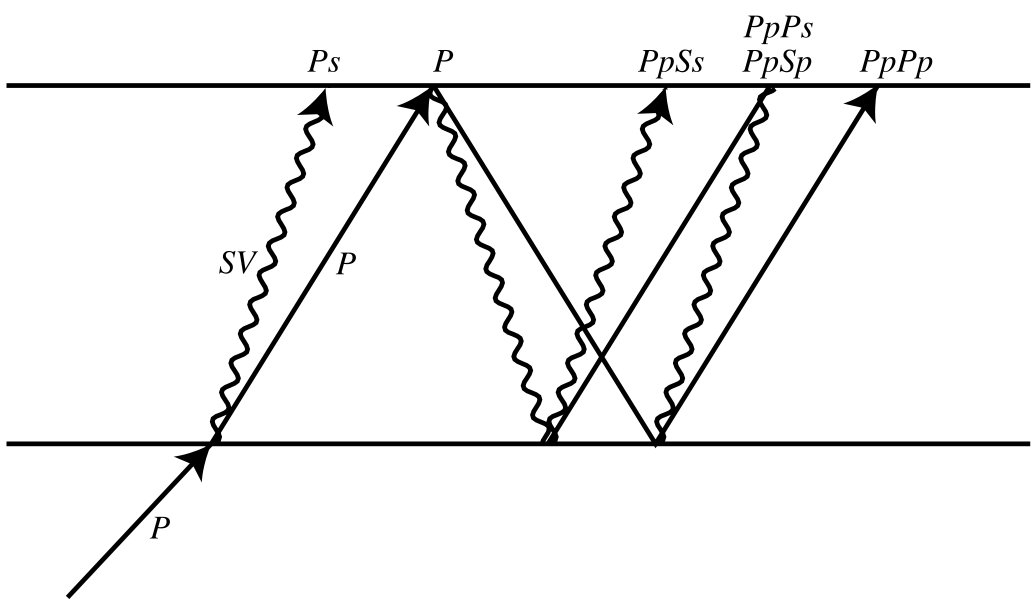


**Figure 7.13** An upcoming $P$ wave incident on a near-surface velocity discontinuity will generate a number of first-order converted and reflected phases.

earthquake as modified by attenuation along the ray path), and thus, just as in the vibroseis example discussed above, *Ps* can often be revealed by deconvolving the $P$ pulse from the rest of the seismogram. The deconvolved waveform is termed the receiver function. For the steeply incident ray paths of distant teleseisms, $P$ appears most strongly on the vertical component and *Ps* on the radial component. Thus, the simplest approach extracts the direct $P$ pulse from the vertical channel and performs the deconvolution on the radial component. However, somewhat cleaner results can be obtained by applying a transformation to estimate the upcoming $P$ and $SV$ wave field from the observed vertical and radial components. This transformation must include the effect of the free-surface reflected phases (i.e., the downgoing $P$ and $SV$ pulses) on the observed displacement at the surface.

Following Kennett (1991) and Bostock (1998), we may express the upcoming $P$ and $SV$ components at the surface as

$$\begin{bmatrix} P \\ SV \end{bmatrix} = \begin{bmatrix} p\beta^2/\alpha & (1-2\beta^2 p^2)/2\alpha\eta_\alpha \\ (1-2\beta^2 p^2)/2\beta\eta_\beta & -p\beta \end{bmatrix} \begin{bmatrix} U_R \\ U_Z \end{bmatrix}, \tag{7.34}$$

where $U_R$ and $U_Z$ are the radial and vertical components, $p$ is the ray parameter, $\alpha$ and $\beta$ are the $P$ and $S$ velocities at the surface, and the $P$ and $S$ vertical slownesses are given by $\eta_\alpha = \sqrt{\alpha^{-2} - p^2}$ and $\eta_\beta = \sqrt{\beta^{-2} - p^2}$. Note that here we adopt the sign convention, opposite to that in Bostock (1998), that the incident $P$ wave has the same polarity on the vertical and radial seismometer components.

This transformation has been applied to the vertical and radial channels in Figure 7.14 and shows how the resulting $P$ and $SV$ components isolate the different phases. In particular, note that the direct $P$ arrival appears only on the $P$ component, while *Ps* appears only on the $SV$ component. The reverberated phases are seen separately on the $P$ and $S$ components according to whether the upcoming final leg beneath the receiver is $P$ or $SV$. The resulting receiver function is plotted at the bottom of Figure 7.14, and in this case has pulses at times given by the differential times of *Ps*, *PpPs* and *PpSs* with respect to the direct $P$ arrival. In general, the receiver-function pulse shapes are more impulsive and symmetric than that of the $P$ waveform, but their exact shape will depend on the deconvolution method and the bandwidth of the data.

Analysis of receiver functions is similar to reflection seismology in many respects. Both methods study seismic phases resulting from velocity jumps at interfaces beneath receivers and require knowledge of the background seismic velocities to translate the timing of these phases into depth. Both often use deconvolution and stacking to improve the signal-to-noise ratio of the results. When closely spaced seismic receivers are available (for example, a seismometer array), migration methods can be used to image lateral variations in structure and correct for scattering

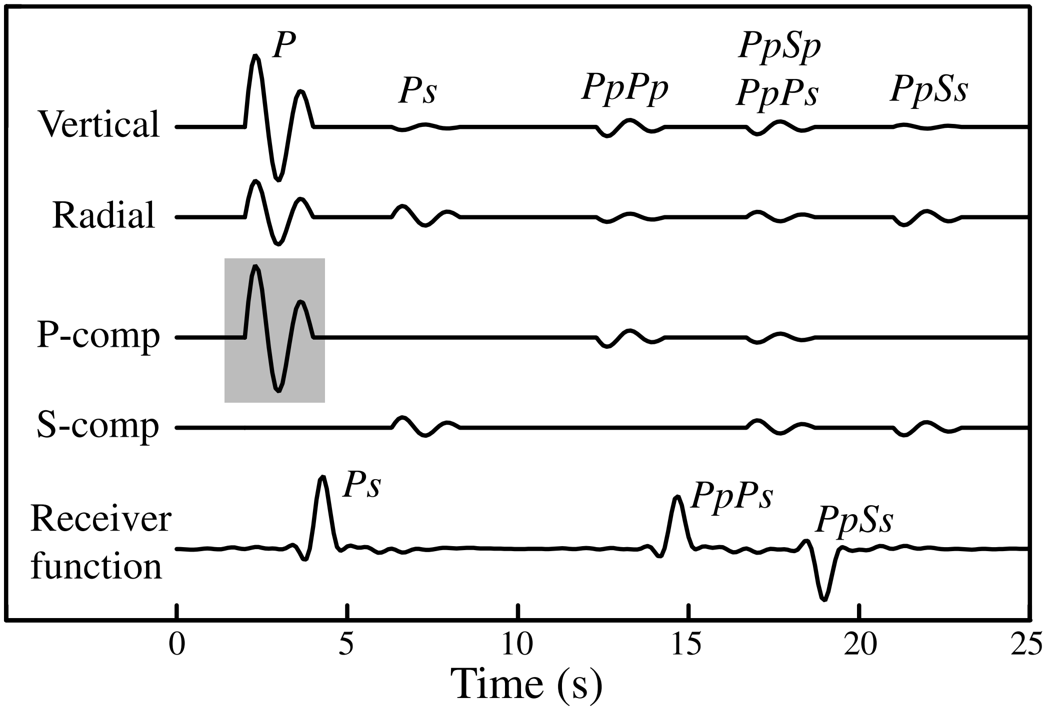


**Figure 7.14** Seismograms showing the response of a simple model of a 35 km thick crust to an upcoming mantle *P* wave. The bottom trace shows the receiver function computed by deconvolving the windowed *P* pulse on the *P*-component trace from the *S*-component trace. The time scale for the top four traces is the same, but the receiver function timing is relative to the *P* arrival, which is why the receiver function pulses are shifted compared to the pulses in the other traces.

artifacts. However, receiver function analysis is complicated by the multiple arrivals generated by single interfaces (see Figure 7.14), and when several discontinuities are present at different depths, it can be difficult to separate out the effects of *Ps* phases from possible reverberations from shallower discontinuities.

If results are available for sources at different epicentral distances from the receiver (i.e., which will arrive at different ray parameters), it is sometimes possible to distinguish the reverberated phases from *Ps* by noting their different moveout with distance. In particular, the differential time $T_{Ps} - T_P$ shrinks with epicentral distance (i.e., decreasing ray parameter) while $T_{PpPs} - T_P$ and $T_{PpSs} - T_P$ increase with epicentral distance. For shallow discontinuities (less than about 150 km), the timing of these arrivals can safely be computed using a plane-wave approximation for the incident *P* wave, which assumes that all of the arrivals have the same ray parameter. However, for deeper features, such as the transition-zone discontinuities near 410 and 660 km depth, the curvature of the wavefront should be taken into account (Lawrence and Shearer, 2006).

The *P*-to-*SV* converted *Ps* phase is sensitive almost entirely to the *S* velocity jump at interfaces, whereas the reverberated phases are also sensitive to the *P*

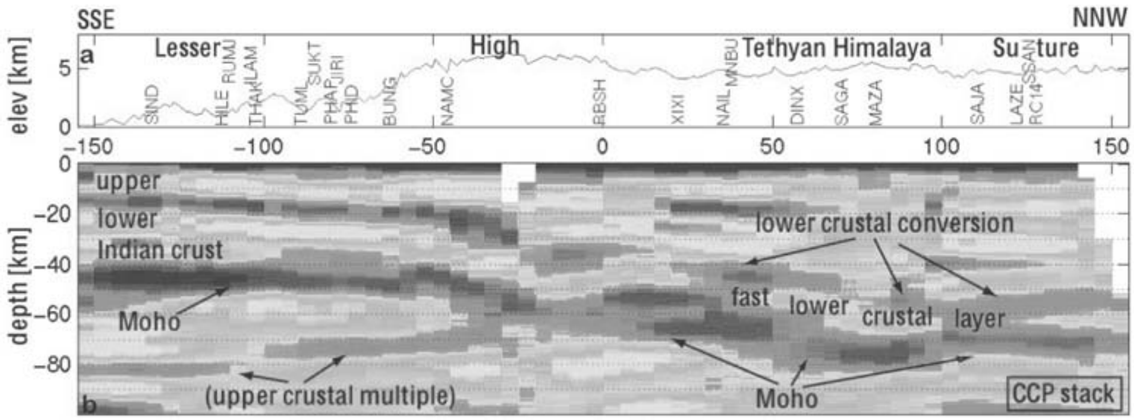


**Figure 7.15** A cross-section of the Himalayan crust, produced from a common conversion point (CCP) stack of receiver functions computed for a line of seismic stations crossing Nepal. A clear Moho conversion is seen, indicating that the crustal thickness increases from ~45 km under India to ~75 km beneath Tibet. Figure adapted from Schulte-Pelkum *et al.* (2005).

velocity and density jumps. Thus, in principle integrated analysis of the complete $P$ coda wavefield can provide much more information than simple receiver function studies of $Ps$ alone. Bostock *et al.* (2001) describe a theory for how this can be done to image crust and upper-mantle structure by processing three-component data from seismic arrays.

Receiver functions have become one of the most popular methods in the global seismologist's toolbox because they are relatively simple to compute and can provide valuable results even from only a single station. They have been used to resolve crustal thickness and depths to the 410 and 660 km discontinuities beneath seismic stations all over the world, and, in subduction zones, to resolve the top of the subducting slab. Where seismic arrays are present, often from temporary seismic experiments, they can produce dramatic images of crust and lithospheric structure as illustrated in Figure 7.15 for a cross-section under the Himalayas.

## 7.7 Kirchhoff theory†

A more rigorous treatment of Huygens' principle was given by Kirchhoff and forms the basis for a number of important techniques for computing synthetic seismograms. Descriptions of applications of Kirchhoff methods to seismology may be found in Scott and Helmberger (1983) and Kampmann and Müller (1989). Kirchhoff theory was first developed in optics and our derivation until equation (7.56) largely follows that of Longhurst (1967). Consider the scalar wave equation (e.g., equation (3.31) where $\phi$ is the $P$-wave potential)

$$\nabla^2 \phi = \frac{1}{c^2} \frac{\partial^2 \phi}{\partial t^2}, \tag{7.35}$$

where $c$ is the wave velocity. Now assume a harmonic form for $\phi$, that is, at a particular frequency $\omega$ we have the monochromatic function

$$\phi = \psi(\mathbf{r}) e^{-i\omega t} = \psi(\mathbf{r}) e^{-ikct}, \tag{7.36}$$

where $\mathbf{r}$ is the position and $k = \omega/c$ is the wavenumber. Note that we have separated the spatial and temporal parts of $\phi$. We then have

$$\nabla^2 \phi = e^{-ikct} \nabla^2 \psi \tag{7.37}$$

and

$$\frac{\partial^2 \phi}{\partial t^2} = -k^2 c^2 \psi e^{-ikct} \tag{7.38}$$

and (7.35) becomes

$$\nabla^2 \psi = -k^2 \psi. \tag{7.39}$$

This is a time-independent wave equation for the space-dependent part of $\phi$. It is also sometimes termed the Helmholtz equation.

Next, recall Green's theorem from vector calculus. If $\psi_1$ and $\psi_2$ are two continuous single-valued functions with continuous derivatives, then for a closed surface $S$

$$\int_V (\psi_2 \nabla^2 \psi_1 - \psi_1 \nabla^2 \psi_2)\, dv = \int_S \left( \psi_2 \frac{\partial \psi_1}{\partial n} - \psi_1 \frac{\partial \psi_2}{\partial n} \right) dS, \tag{7.40}$$

where the volume integral is over the volume enclosed by $S$, and $\partial/\partial n$ is the derivative with respect to the outward normal vector to the surface. Now assume that both $\psi_1$ and $\psi_2$ satisfy (7.39), that is,

$$\nabla^2 \psi_1 = -k^2 \psi_1, \tag{7.41}$$

$$\nabla^2 \psi_2 = -k^2 \psi_2. \tag{7.42}$$

In this case, the left part of (7.40) vanishes and the surface integral must be zero:

$$\int_S \left( \psi_2 \frac{\partial \psi_1}{\partial n} - \psi_1 \frac{\partial \psi_2}{\partial n} \right) dS = 0. \tag{7.43}$$

Now suppose that we are interested in evaluating the disturbance at the point $P$, which is enclosed by the surface $S$ (Fig. 7.16). We set $\psi_1 = \psi$, the amplitude of

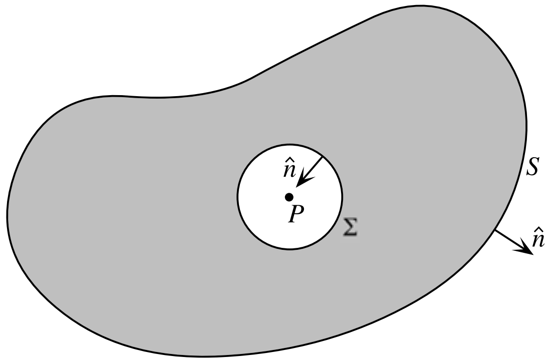


**Figure 7.16** A point $P$ surrounded by a surface $S$ of arbitrary shape. Kirchhoff's formula is derived by applying Green's theorem to the volume between $S$ and an infinitesimal sphere $\Sigma$ surrounding $P$.

the harmonic disturbance. We are free to choose any function for $\psi_2$, provided it also satisfies (7.39). It will prove useful to define $\psi_2$ as

$$\psi_2 = \frac{e^{ikr}}{r}, \tag{7.44}$$

where $r$ is the distance from $P$. This function has a singularity at $r = 0$ and so the point $P$ must be excluded from the volume integral for Green's theorem to be valid. We can do this by placing a small sphere $\Sigma$ around $P$. Green's theorem may now be applied to the volume between $\Sigma$ and $S$; these surfaces, together, make up the integration surface. On the surface of the small sphere the outward normal to this volume is opposite to the direction of $r$ and thus $\partial/\partial n$ can be replaced with $-\partial/\partial r$ and the surface integral over $\Sigma$ may be expressed as

$$\begin{aligned}\int_\Sigma \left(\psi_2 \frac{\partial \psi}{\partial n} - \psi \frac{\partial \psi_2}{\partial n}\right) dS &= \int_\Sigma \left[\frac{-e^{ikr}}{r}\frac{\partial \psi}{\partial r} + \psi \frac{\partial}{\partial r}\left(\frac{e^{ikr}}{r}\right)\right] dS \\ &= \int_\Sigma \left[\frac{-e^{ikr}}{r}\frac{\partial \psi}{\partial r} + \psi \left(\frac{-e^{ikr}}{r^2} + \frac{ike^{ikr}}{r}\right)\right] dS.\end{aligned} \tag{7.45}$$

Now let us change this to an integral over solid angle $\Omega$ from the point $P$, in which $dS$ on $\Sigma$ subtends $d\Omega$ and $dS = r^2\, d\Omega$. Then

$$\int_\Sigma = \int_{\text{around } P} \left(-re^{ikr}\frac{\partial \psi}{\partial r} - \psi e^{ikr} + rik\psi e^{ikr}\right) d\Omega. \tag{7.46}$$

Now consider the limit as $r$ goes to zero. Assuming that $\psi$ does not vanish, then only the second term in this expression survives. Thus as $r \to 0$

$$\int_\Sigma \to \int -\psi e^{ikr} d\Omega. \tag{7.47}$$

As the surface $\Sigma$ collapses around $P$, the value of $\psi$ on the surface may be assumed to be constant and equal to $\psi_P$, its value at $P$. Thus

$$\int_\Sigma \rightarrow \int -\psi_P e^{ikr} d\Omega \tag{7.48}$$

$$= -\psi_P \int e^{ikr} d\Omega \tag{7.49}$$

$$= -\psi_P \int d\Omega \text{ since } e^{ikr} \rightarrow 1 \text{ as } r \rightarrow 0 \tag{7.50}$$

$$= -4\pi\psi_P. \tag{7.51}$$

From (7.43) we know that $\int_{S+\Sigma} = 0$, so we must have $\int_S = +4\pi\psi_P$, or

$$4\pi\psi_P = \int_S \left[ \frac{e^{ikr}}{r} \frac{\partial\psi}{\partial n} - \psi \frac{\partial}{\partial n} \left( \frac{e^{ikr}}{r} \right) \right] dS \tag{7.52}$$

$$= \int_S \left[ \frac{e^{ikr}}{r} \frac{\partial\psi}{\partial n} - \psi e^{ikr} \frac{\partial}{\partial n} \left( \frac{1}{r} \right) - \frac{ik\psi e^{ikr}}{r} \frac{\partial r}{\partial n} \right] dS, \tag{7.53}$$

since $\frac{\partial}{\partial n} = \frac{\partial}{\partial r}\frac{\partial r}{\partial n}$. This is often called Helmholtz's equation. Since $\phi = \psi e^{-ikct}$ (7.35), we have

$$\psi = \phi e^{ikct} \tag{7.54}$$

and (7.53) becomes

$$\begin{aligned} \phi_P &= \frac{1}{4\pi} e^{-ikct} \int_S \left[ \frac{e^{ikr}}{r} \frac{\partial\psi}{\partial n} - \psi e^{ikr} \frac{\partial}{\partial n} \left( \frac{1}{r} \right) - \frac{ik\psi e^{ikr}}{r} \frac{\partial r}{\partial n} \right] dS \\ &= \frac{1}{4\pi} \int_S \left[ \frac{e^{-ik(ct-r)}}{r} \frac{\partial\psi}{\partial n} - \psi e^{-ik(ct-r)} \frac{\partial}{\partial n} \left( \frac{1}{r} \right) - \frac{ik\psi e^{-ik(ct-r)}}{r} \frac{\partial r}{\partial n} \right] dS. \end{aligned} \tag{7.55}$$

This expression gives $\phi(t)$ at the point $P$. Note that the term $\psi e^{-ik(ct-r)} = \psi e^{-ikc(t-r/c)}$ is the value of $\phi$ at the element $dS$ at the time $t - r/c$. This time is referred to as the *retarded value* of $\phi$ and is written $[\phi]_{t-r/c}$. In this way, we can express (7.55) as

$$\phi_P = \frac{1}{4\pi} \int_S \left( \frac{1}{r} \left[ \frac{\partial\phi}{\partial n} \right]_{t-r/c} - \frac{\partial}{\partial n} \left( \frac{1}{r} \right) [\phi]_{t-r/c} + \frac{1}{cr} \frac{\partial r}{\partial n} \left[ \frac{\partial\phi}{\partial t} \right]_{t-r/c} \right) dS, \tag{7.56}$$

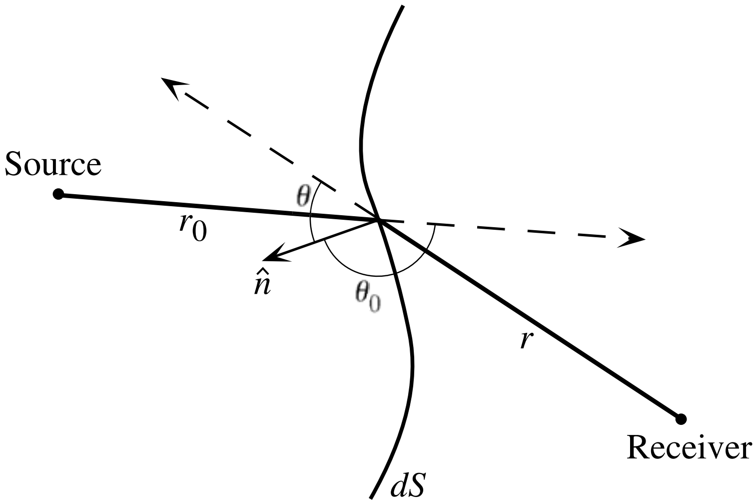


**Figure 7.17** The ray geometry for a single point on a surface *dS* separating a source and receiver.

where we have used $\partial\phi/\partial t = -ikc\psi e^{-ikct}$. Equation (7.56) is a standard form for what is often termed Kirchhoff's formula; it is found in many optics textbooks and is also given in Scott and Helmberger (1983). We see that the disturbance at $P$ can be computed from the conditions of $\phi$ over a closed surface surrounding $P$ where $r/c$ represents the time taken for the disturbance to travel the distance $r$ from $dS$ to $P$. We need to know both the value of $\phi$ and its normal derivative on $dS$ to compute this integral.

This is not an especially convenient form to use directly in most seismic applications. Suppose the value of $\phi$ at each point on the surface could be obtained from a source time function $f(t)$ a distance $r_0$ from $dS$. Then on $dS$ we have

$$\phi = \frac{1}{r_0} f(t - r_0/c), \tag{7.57}$$

$$\frac{\partial\phi}{\partial t} = \frac{1}{r_0} f'(t - r_0/c), \tag{7.58}$$

where the $1/r_0$ term comes from the geometrical spreading of the wavefront.

If $\theta_0$ and $\theta$ are the angles of the incoming and outgoing ray paths from the surface normal (Fig. 7.17), then

$$\frac{\partial r_0}{\partial n} = \cos\theta_0 \quad \text{and} \quad \frac{\partial r}{\partial n} = \cos\theta, \tag{7.59}$$

$$\frac{\partial\phi}{\partial n} = \frac{\partial\phi}{\partial r_0}\frac{\partial r_0}{\partial n} \tag{7.60}$$

$$= \frac{\partial\phi}{\partial r_0}\cos\theta_0, \tag{7.61}$$

and

$$\frac{\partial}{\partial n}\left(\frac{1}{r}\right) = \frac{\partial r}{\partial n}\frac{\partial}{\partial r}\left(\frac{1}{r}\right) \tag{7.62}$$

$$= -\frac{1}{r^2}\cos\theta. \tag{7.63}$$

We can evaluate $\partial\phi/\partial r_0$ using the chain rule:

$$\frac{\partial}{\partial r_0}\left(\frac{1}{r_0}f(t-r_0/c)\right) = -\frac{1}{r_0^2}f(t-r_0/c) - \frac{1}{cr_0}f'(t-r_0/c) \tag{7.64}$$

since $\frac{\partial}{\partial r_0} = \frac{\partial t}{\partial r_0}\frac{\partial}{\partial t} = -\frac{1}{c}\frac{\partial}{\partial t}$. Putting (7.57)–(7.64) into (7.56), we have

$$\begin{aligned}\phi_P(t) &= \frac{1}{4\pi}\int_S\left(\frac{-1}{rr_0^2}\cos\theta_0 + \frac{1}{r^2 r_0}\cos\theta\right) f(t-r/c-r_0/c)\,dS \\ &\quad + \frac{1}{4\pi}\int_S\left(\frac{-1}{crr_0}\cos\theta_0 + \frac{1}{crr_0}\cos\theta\right) f'(t-r/c-r_0/c)\,dS.\end{aligned} \tag{7.65}$$

The negative signs arise from our definition of $\hat{n}$ in the direction opposing $r_0$; these terms are positive since $\cos\theta_0$ is negative. Equation (7.65) may also be expressed in terms of convolutions with $f(t)$ and $f'(t)$:

$$\begin{aligned}\phi_P(t) &= \frac{1}{4\pi}\int_S \delta\left(t-\frac{r+r_0}{c}\right)\left(\frac{-1}{rr_0^2}\cos\theta_0 + \frac{1}{r^2 r_0}\cos\theta\right) dS * f(t) \\ &\quad + \frac{1}{4\pi}\int_S \delta\left(t-\frac{r+r_0}{c}\right)\left(\frac{-1}{crr_0}\cos\theta_0 + \frac{1}{crr_0}\cos\theta\right) dS * f'(t).\end{aligned} \tag{7.66}$$

Notice that the $f(t)$ terms contain an extra factor of $1/r$ or $1/r_0$. For this reason they are most important close to the surface of integration and can be thought of as near-field terms. In practice, the source and receiver are usually sufficiently distant from the surface (i.e., $\lambda \ll r, r_0$) that $\phi_P$ is well approximated by using only the far-field $f'(t)$ terms. In this case we have

$$\phi_P(t) = \frac{1}{4\pi c}\int_S \delta\left(t-\frac{r+r_0}{c}\right)\frac{1}{rr_0}(-\cos\theta_0 + \cos\theta)\,dS * f'(t). \tag{7.67}$$

This formula is the basis for many computer programs that compute Kirchhoff synthetic seismograms.

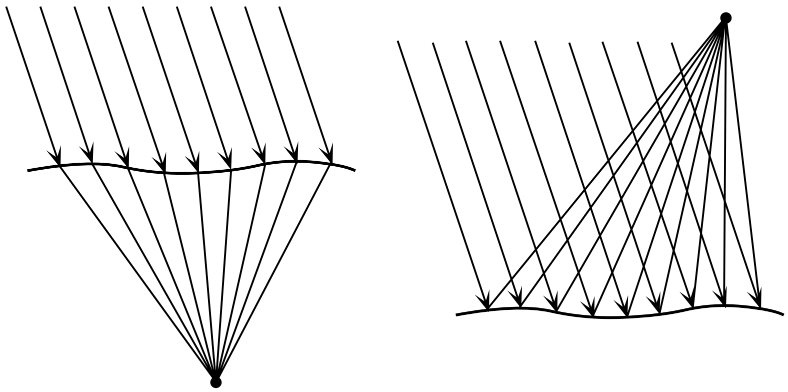

**Figure 7.18** Kirchhoff theory can be used to compute the effect of an irregular boundary on both transmitted and reflected waves.

### 7.7.1 Kirchhoff applications

Probably the most common seismic application of Kirchhoff theory involves the case of an irregular interface between simpler structure on either side. Kirchhoff theory can be used to provide an approximate solution for either the transmitted or reflected wavefield due to this interface (Fig. 7.18). For example, we might want to model the effect of irregularities on the core–mantle boundary, the Moho, the sea floor, or a sediment–bedrock interface. In each case, there is a significant velocity contrast across the boundary.

Let us consider the reflected wave generated by a source above an undulating interface. Assume that the incident wavefield is known and can be described with geometrical ray theory. Then we make the approximation that the reflected wavefield just above the interface is given by the plane-wave reflection coefficient for the ray incident on the surface. This approximation is sometimes called the Kirchhoff, physical optics, or tangent plane hypothesis (Scott and Helmberger, 1983). Each point on the surface reflects the incident pulse as if there were an infinite plane tangent to the surface at that point. Considering only the far-field terms, we then have

$$\phi_P(t) = \frac{1}{4\pi c} \int_S \delta\left(t - \frac{r + r_0}{c}\right) \frac{R(\theta_0)}{r r_0} (\cos\theta_0 + \cos\theta)\, dS * f'(t), \qquad (7.68)$$

where $R(\theta_0)$ is the reflection coefficient, $\theta_0$ is the angle between the incident ray and the surface normal, and $\theta$ is the angle between the scattered ray and the surface normal (see Fig. 7.19).

If the overlying layer is not homogeneous, then the $1/r$ and $1/r_0$ terms must be replaced with the appropriate source-to-interface and interface-to-receiver geometrical spreading coefficients. In some cases, particularly for obliquely arriving rays,

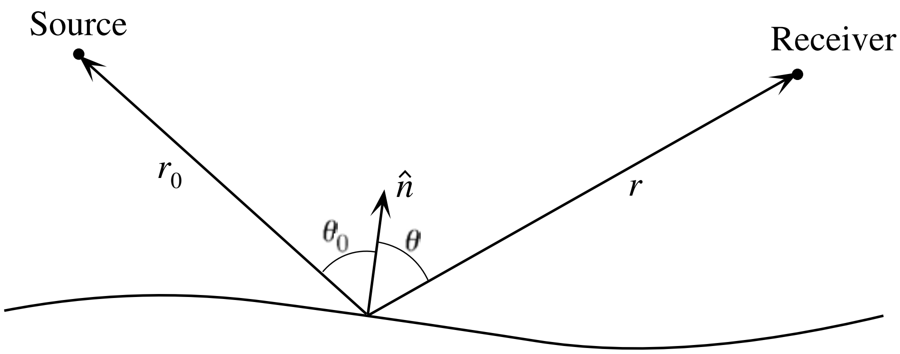


**Figure 7.19** Ray angles relative to the surface normal for a reflected wave geometry.

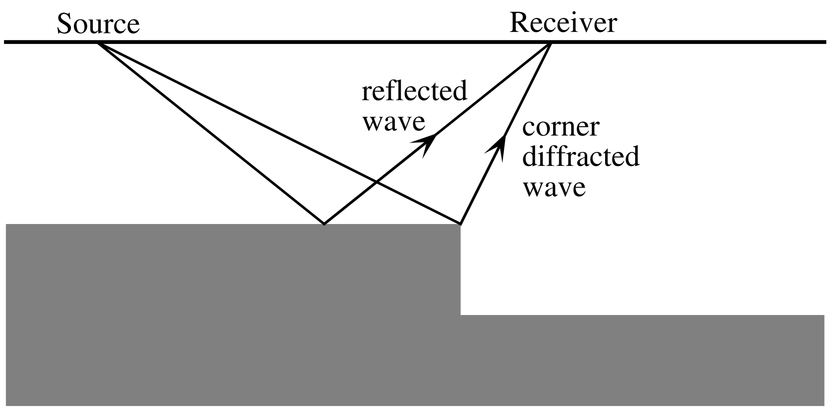


**Figure 7.20** This structure will produce both a direct reflected pulse and a diffracted pulse for the source–receiver geometry shown.

the reflection coefficient $R$ may become complex. If this occurs, then this equation will have both a real and an imaginary part. The final time series is obtained by adding the real part to the Hilbert transform of the imaginary part.

The Kirchhoff solution will correctly model much of the frequency dependence and diffracted arrivals in the reflected wavefield. These effects are not obtained through geometrical ray theory alone, even if 3-D ray tracing is used. For example, consider a source and receiver above a horizontal interface containing a vertical fault (Fig. 7.20). Geometrical ray theory will produce only the main reflected pulse from the interface, while Kirchhoff theory will provide both the main pulse and the secondary pulse diffracted from the corner. However, Kirchhoff theory also has its limitations, in that it does not include any multiple scattering or diffractions along the interface; these might be important in more complicated examples.

### 7.7.2 How to write a Kirchhoff program

As an illustration, let us list the steps involved in writing a hypothetical Kirchhoff computer program to compute the reflected wavefield from a horizontal interface with some irregularities.

1. Specify the source and receiver locations.
2. Specify the source-time function $f(t)$.
3. Compute $f'(t)$, the derivative of the source-time function.
4. Initialize to zero a time series $J(t)$, with sample interval $dt$, that will contain the output of the Kirchhoff integral.
5. Specify the interface with a grid of evenly spaced points in $x$ and $y$. At each grid point, we must know the height of the boundary $z$ and the normal vector to the surface $\hat{n}$. We also require the surface area, $dA$, corresponding to the grid point. This is approximately $dx\,dy$ where $dx$ and $dy$ are the grid spacings in the $x$ and $y$ directions, respectively (if a significant slope is present at the grid point, the actual surface area is greater and this correction must be taken into account). The grid spacing should be finer than the scale length of the irregularities.
6. At each grid point, trace rays to the source and receiver. Determine the travel times to the source and receiver, the ray angles to the local normal vector ($\theta_0$ and $\theta$), and the geometrical spreading factors $g_0$ (source-to-surface) and $g$ (surface-to-receiver).
7. At each grid point, compute the reflection coefficient $R(\theta_0)$ and the factor $\cos\theta_0 + \cos\theta$.
8. At each grid point, compute the product $R(\theta_0)(\cos\theta_0 + \cos\theta)dA/(4\pi c g_0 g)$. Add the result to the digitized point of $J(t)$ that is closest to the total source-surface-receiver travel time, after first dividing the product by the digitization interval $dt$.
9. Repeat this for all grid points that produce travel times within the time interval of interest.
10. Convolve $J(t)$ with $f'(t)$, the derivative of the source-time function, to produce the final synthetic seismogram.
11. (very important) Repeat this procedure at a finer grid spacing, $dx$ and $dy$, to verify that the same result is obtained. If not, the interface is undersampled and a finer grid must be used.

Generally the $J(t)$ function will contain high-frequency numerical “noise” that is removed through the convolution with $f'(t)$. It is computationally more efficient to compute $f'(t)$ and convolve with $J(t)$ than to compute $J'(t)$ and convolve with $f(t)$, particularly when multiple receiver positions are to be modeled.

### 7.7.3 Kirchhoff migration

Kirchhoff results can be used to implement migration methods for reflection seismic data that are consistent with wave propagation theory. For zero-offset data, $\theta_0 = \theta$

and $r_0 = r$ and (7.68) becomes

$$\phi_P(t) = \frac{1}{2\pi c} \int_S \delta\left(t - \frac{r + r_0}{c}\right) \frac{R(\theta_0)}{r^2} \cos\theta \, dS * f'(t). \tag{7.69}$$

To perform the migration, the time derivative of the data is taken and the traces for each hypothetical scattering point are multiplied by the obliquity factor $\cos\theta$, scaled by the spherical spreading factor $1/r^2$ and then summed along the diffraction hyperbolas.

## 7.8 Exercises

1. (COMPUTER) Recall equation (7.17) for the vibroseis sweep function:

$$v(t) = A(t) \sin[2\pi(f_0 + bt)t].$$

   (a) Solve for $f_0$ and $b$ in the case of a 20-s long sweep between 1 and 4 Hz. Hint: $b$ = 3/20 is incorrect! Think about how rapidly the phase changes with time.
   (b) Compute and plot $v(t)$ for this sweep function. Assume that $A(t) = \sin^2(\pi t/20)$ (this is termed a Hanning taper; note that it goes smoothly to zero at $t = 0$ and $t = 20$ s). Check your results and make sure that you have the right period at each end of the sweep.
   (c) Compute and plot the autocorrelation of $v(t)$ between $-2$ and 2 s.
   (d) Repeat (b) and (c), but this time assume that $A(t)$ is only a short 2-s long taper at each end of the sweep, that is, $A(t) = \sin^2(\pi t/4)$ for $0 < t < 2$, $A(t) = 1$ for $2 \le t \le 18$, and $A(t) = \sin^2[\pi(20 - t)/4]$ for $18 < t < 20$. Note that this milder taper leads to more extended sidelobes in the autocorrelation function.
   (e) What happens to the pulse if autocorrelation is applied a second time to the autocorrelation of $v(t)$? To answer this, compute and plot $[v(t) \star v(t)] \star [v(t) \star v(t)]$ using $v(t)$ from part (b). Is this a way to produce a more impulsive wavelet?

2. A reflection seismic experiment produces the CMP gather plotted in Figure 7.21. Using the $t^2(x^2)$ method, determine the approximate rms velocity of the material overlying each reflector. Then compute an approximate depth to each reflector. Note: You should get approximately the same velocity for each reflector; do not attempt to solve for different velocities in the different layers.

3. Consider a simple homogeneous layer over half-space model (as plotted in Fig. 7.22) with $P$ velocity $\alpha_1$ and $S$ velocity $\beta_1$ in the top layer and $P$ velocity $\alpha_2$ in the bottom layer.